Wavefront sensors for optical diagnostics in fluid mechanics: application to heated flow, turbulence and droplet evaporation

D. R. Neal, T. J. O'Hern, J.R. Torczynski, M. E. Warren and R. Shul
Sandia National Laboratories, Albuquerque, New Mexico 87185-5800
T. S. McKechnie, *POD Associates, Albuquerque, New Mexico 87106*

ABSTRACT

Optical measurement techniques are extremely useful in fluid mechanics because of their non-invasive nature. However, it is often difficult to separate measurement effects due to pressure, temperature and density in real flows. Using a variation of a Shack-Hartmann wavefront sensor, we have made wavefront measurements that have extremely large dynamic range coupled with excellent sensitivity at high temporal and spatial resolution. These wavefront variations can be directly related to density perturbations in the fluid. We have examined several classes of flow including volumetrically heated gas, grid turbulence and droplet evaporation.

1. INTRODUCTION

Many different types of optical diagnostics have been applied to measurements in fluid mechanics. These include schlieren, interferometry[1], laser-induced fluorescence[2], photorefractive effect[3], Raman scattering, laser doppler velocimetry, shadowgraph, and non-linear optics techniques. These various methods have been applied to measure the pressure, temperature, species concentration, density, velocity, and particle distributions of many different types of flows. However, in many cases, it is difficult to separate one effect from another. For example, in laser induced fluorescence (LIF), it is difficult to separate pressure and density effects since the LIF signal depends strongly on both[4]. Alternately, it is difficult to design an optical diagnostic system that responds to the large variations in density and pressure in combustion and high speed flow systems, while also resolving turbulence in these same environments. Techniques such as interferometry, that are sensitive to small perturbations, cannot do so in the presence of large density gradients. No one technique will likely ever supplant the variety of measurements needed to fully quantify all flows of interest. However, the application of Shack-Hartmann wavefront sensing to fluid diagnostics using high speed CCD sensors can be shown to overcome some of these problems.

Shack-Hartmann sensing has been used extensively in optical fabrication and testing, astronomy, adaptive optics, and laser beam control[5, 6]. The Shack-Hartmann sensor is used to measure the wavefront of a beam of light (not necessarily a laser). It consists of an array of lenses that focus onto a detector array capable of measuring the position of the focused light. With the detector at the focal position, the focal spot position is independent of the intensity pattern across the subaperture, and depends only on the average slope of the wavefront. With many subapertures, the incident wavefront can be reconstructed by spatial integration. For fluid mechanics problems, usually a laser is used to probe the flow under study, with density variations causing perturbations of the index of refraction of the medium. In turn, these index of refraction variations lead to variations in the laser wavefront. The Shack-Hartmann sensor is used to determine these variations. Since the index of refraction usually depends strongly on the density of the fluid and only weakly upon temperature, it can be used to measure the density independent of other variations in the flow. In fact, we have applied this technique to measurement of nuclear-reactor-heated flows where the temperature, pressure and density all varied greatly, and have found that we can make measurements of the density alone with good success[7].

There have been several recent advances that have made possible the development of useful wavefront sensors. These include the development of fast CCD area and line scan cameras, the development of micro-lens array manufacturing technology, and the improvement in computer data acquisition and processing equipment.

One common embodiment of a Shack-Hartmann wavefront sensor uses discrete lenslets and quadrant cell detectors to make a limited number of measurements across the field[6]. These sensors have the advantage of extremely high speed because of the many parallel connections, but have significantly reduced dynamic range, are complicated by the large numbers of connections and electronics, and usually have limited net resolution. They are useful for closed-loop adaptive optics systems where dynamic range is controlled by a deformable mirror. They can be used for fluid mechanics measurements only for limited dynamic range effects or in massively complicated adaptive optics facilities.

0-8194-1254-6/93/$6.00

Another technique is to use a CCD camera coupled to a lenslet array to simplify the construction of the wavefront sensor. With modern cameras this is a technique that is used extensively in astronomy and other adaptive optics systems[5, 8, 9]. However, as the number of subapertures grows, it becomes necessary to sacrifice either bandwidth, resolution, dynamic range, or dimensionality. For adaptive optics systems, the deformable mirror can be used to extend the dynamic range, and some of these compromises can be avoided. However, a deformable mirror is extremely expensive and complicated, and is not likely to be applied to laboratory fluid mechanics measurements.

The compromise we have chosen is to reduce the measurement from two dimensions to one. This greatly reduces the number of pixels required for a single measurement, and for a fixed pixel bandwidth, thereby increasing the measurement bandwidth of the system. More pixels per line can be used for the same frame rate, thus more lenslets can be focused onto the detector without cross talk. We have selected fairly long focal length lenslet arrays with moderate spatial resolution which leads to an extremely large dynamic range and excellent sensitivity. The one-dimensional device also greatly simplifies the construction of the lenslet array, allowing the use of a stack of small cylindrical lenses made with conventional optical construction techniques. Alignment sensitivity is also improved, because of both the large dynamic range, and the insensitivity to out-of-plane disturbances.

The body of this paper discusses the design of a variety of these one-dimensional wavefront sensors, applications to several different flows, and enhancements that are under development at Sandia.

2. WAVEFRONT SENSOR DESIGN

The design of a wavefront sensor is driven by several different quantities: temporal and spatial bandwidth, dimensionality, resolution, and dynamic range. For CCD type sensors where the information is obtained sequentially, these parameters are often interrelated. For example, a large pixel count detector can be used to provide high spatial resolution or dynamic range, but will lead to lower temporal resolution. The proper wavefront sensor design is driven by the requirements of the application under study. However, it is possible to design wavefront sensors with broad applicability. Some design parameters for one-dimensional and two-dimensional wavefront sensors are given in Table 1.

The use of a one-dimensional sensor instead of a two-dimensional sensor greatly improves the detector bandwidth for a given spatial resolution or dynamic range. For a fixed pixel rate f_p, the sensor bandwidth scales as f_p/N_p for a linear system versus f_p/N_p^2 for a square area sensor

Quantity	1-D WFS	2-D WFS
Frame rate	f_p/N_p	$f_p/(N_x N_y)$
Spatial resolution	d	d
Dynamic range	$N_p/(fd)$	$N_p/(fd)$

Table 1: Parameter definitions for 1-D and 2-D wavefront sensors

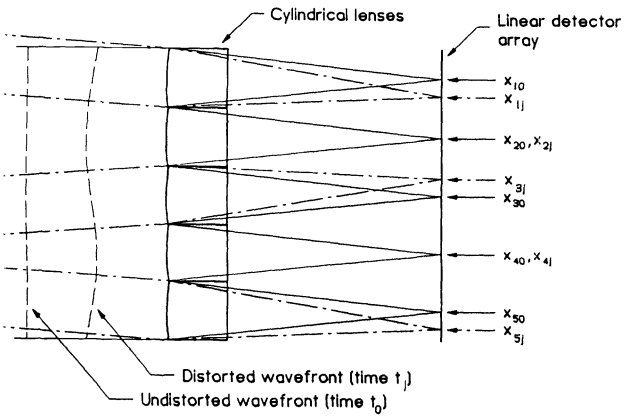

Figure 1: Wavefront sensor design.

where N_p is the number of pixels per row in the camera. Thus for a 512×512 element area camera operating at 20 Mpixels/sec, the frame rate is 76 Hz, whereas for a line-scan camera with 512 pixels, the bandwidth is 39 kHz. Since often this large bandwidth is not needed, the line pixel count can be increased, thereby providing more dynamic range and/or resolution.

We have built wavefront sensors with 10, 20 and 40 elements across a one-inch aperture with 5, 10 and 20 cm focal lengths. These are built around EG&G Reticon diode array cameras with 1024 and 2048 pixels. A typical configuration is shown in Fig. 1.

A typical 20 element sensor can operate at up to about 10 kHz frame rate (although it was used at 2.3 kHz because of data acquisition system limitations), has ± 10 mrad dynamic range, and is sensitive to 0.5 μrad angular variations per subaperture. This corresponds to a change in wavefront error of 1/800 of a wave across the 1/20 inch subaperture.

Data acquisition for our current generation of wavefront sensors consists of a synchronized transient digitizer that is used to record the pixel values. An output is used from the line scan camera that includes a synch pulse. The synch information is presently used by the data analysis software to determine the frame start times (index j). This operation could easily be performed electronically using a synch stripper or a frame grabber card.

Data analysis primarily consists of locating the positions of the peaks, converting this information to wavefront slope information, and then integrating to compute the wavefront. Extensive software has been written to perform this analysis, and to provide for a variety of different displays. Figure 2(a) shows a typical display, with the focal spot peaks and threshold settings evident. The analysis usually consists of the following steps:

1. Locate positions of the focal spots $\hat{x}_{ij}$ using a centroid or other analysis technique. A set of windows is usually defined in which centroids are computed. The window location can be allowed to float based on an automatic tracking scheme, or can be fixed through user adjustment. Figure 2(b) shows a typical screen from this step of the data analysis program. To minimize effects caused by noise that is far from the peak location, a data threshold operation is usually performed. This step can greatly improve the noise rejection of the system.

2. Compute wavefront slopes using the spot positions. The wavefront slope $(\frac{d\phi_j}{dx})_i$ is determined from:

$$\left(\frac{d\phi_j}{dx}\right)_i = \frac{\hat{x}_{ij} - \hat{x}_{i0}}{f} \qquad (1)$$

   where i is the spot position index, j is the time index and f is the lenslet focal length. A typical screen showing this computation (labeled deviation angle) is presented in Fig. 2(c).

3. Once the wavefront slopes have been determined, an integration is sufficient to recover the wavefront ϕ_j. Several display options are available that use different forms of integration, depending on the requirements of accuracy, speed and resolution. Figure 2(d) shows a typical data analysis screen with the wavefront integrated and wavefront slope statistics computed. The analysis program is designed to animate the display for easy interpretation, with simple user control of many scaling and display functions. In addition, three-dimensional plots can be automatically generated and printed by the program through interaction with a commercial 3-D plot routine.

This analysis technique has been proven to be extremely effective for most fluid dynamic measurements. The operator is free to concentrate on the physics of the fluid mechanics, rather than on the specifics of wavefront sensing. A number of calibration steps are available for further refining the data analysis to allow absolute calibration of the sensor ($\hat{x}_{i0}$ is computed from a separate calibration measurement) or provide consistent analysis for several separate measurements.

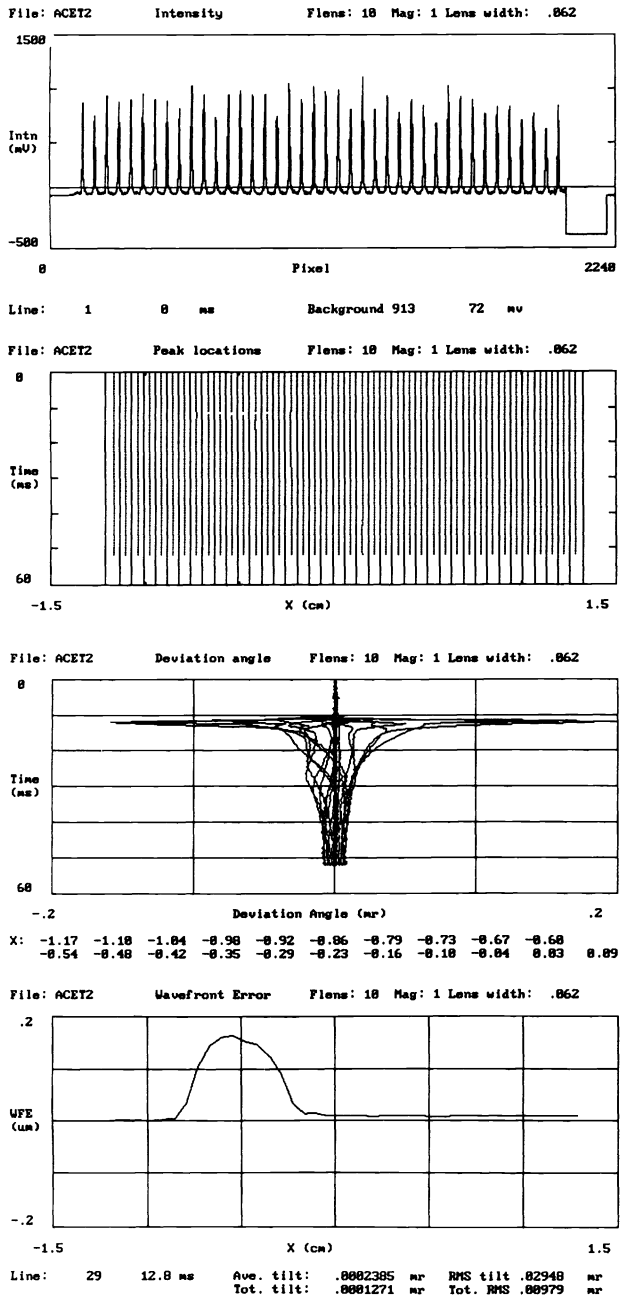

Figure 2: Data analysis program screens. (a) Peaks and threshold, (b) peak centroid finding, (c) wavefront slope calculation, (d) wavefront error data analysis.

With a typical sensor (40 element, 10 cm focal length, 2048 element array) the focal spots are positioned 635 μm or 48 pixels apart. This yields a dynamic range (without automatic spot tracking) of 6.35 mrad (or 6.4 waves per subaperture). In practice we have found that up to 20 mrad dynamic range is usable with spot tracking. For the same sensor, the focal spot occupies about 15 pixels (between the first two zeros of the point spread function). With thresholding, 10 pixels are usually used in the centroid computation. From McKechnie[10], it can be shown that, for a weak aberration across the small subaperture, the location of the brightest point in the point spread function represents the average wavefront slope over the aperture. For these small subapertures, the aberrations are small even for large wavefront gradients. Hence the threshold operation does not degrade the accuracy of the measurement. What it does; is eliminate a significant noise contribution in the calculation that is heavily weighted. An expression for the rms wavefront error, ϕ_{rms}, introduced by photon noise for typical wavefront sensor parameters is:

$$\phi_{\text{rms}} = \frac{d\Delta}{f\pi}\left(\frac{m}{N_0}\right)^{\frac{1}{2}} \qquad (2)$$

where m is the number of pixels involved in the centroid calculation, d is the lenslet diameter, Δ is the pixel width, f is the lenslet focal length and N_0 the number of photo electrons required to saturate the detector. A typical value for this expression is 0.1 to 0.2 nm. Values in the range 0.2–0.3 nm have often been observed experimentally. For a 40 element sensor, this represents 1/5000–1/3000 of a wave (over each 0.635 mm diameter subaperture). Since the wavefront sensor is often used in a mode where the calibration is made a few milliseconds before the measurement, this can often be achieved in practice over the whole one inch aperture. However, the integration process used to reconstruct the wavefront from the wavefront slopes can lead to a substantial increase in the residual wavefront error.

The small aperture size, long lenslet focal length ($f\#$ of 157), and large pixel count wavefront sensor combine to yield an extremely large dynamic range, low noise, high bandwidth sensor.

3. APPLICATIONS

This section describes three applications that are typical for this wavefront sensor. The first is the measurement of very large wavefront errors induced by a nuclear-heated flow, the second is the application of wavefront sensing to very weak grid turbulence in a heated-gas wind tunnel, and the third is the measurement of vapor concentrations surrounding falling evaporating droplets.

3.1 Nuclear-reactor-heated flow

If fissionable material is irradiated by neutrons from a nuclear reactor, the fission fragments thus produced can be used directly to excite (pump) atomic and molecular lasing states in gaseous species, with the resulting device termed a nuclear-reactor-pumped laser (see Torczynski and Neal[7] for an extensive bibliography of this topic). During this process, some of the energy deposited in the gas appears as heat. This volumetric heating is time-varying, spatially nonuniform, and large enough to induce appreciable gas motion, which results in appreciable density gradients normal to the optical axis of the laser. Thus a probe laser beam passing through the laser cell experiences a temporally-varying wavefront perturbation that can be directly measured with the wavefront sensor discussed in the previous sections. Torczynski and Neal[7] report the results of an experimental study of this type, and include comparisons to a numerical model of the gas motion induced by the transient heating. As an illustration of the wavefront sensor technique, the major results of their work are summarized below.

Torczynski and Neal[7] examined six sets of conditions, summarized in Tables 2 and 3. The rectangular laser cell used in the experiments (see Fig. 3) had internal dimensions of 1.5 cm×7 cm×60 cm, and the connected unheated volume into which gas can flow during heating (fill lines, etc.) comprised 15% of the total internal volume. In all cases, the gas mixture was composed of 99.5% argon and 0.5% xenon, with an initial temperature of 300 K. The total initial gas pressure (the sum of the partial pressures shown in Table 2) ranged from 52 to 416 kPa. The heating was produced by 0.91-μm-thick enriched UO_2 foils on the 7 cm × 60 cm walls. Two different neutron pulses are used to induce the heating: a "weak" pulse and a "strong" pulse (see Table 3), both of which are well described by the Gaussian form $h(t) = Q_0 \exp\{-[(t - t_p)/t_s]^2\}$. The strong pulse is five times the amplitude of the weak pulse, but lasts only half as long. The actual gas heating is determined by multiplying $h(t)$ by a function that depends both on x and on the gas density field[7].

Expt.	Pulse	p_{Ar} (kPa)	p_{Xe} (kPa)
A4435	Weak	51.7	0.259
A4438	Weak	103.4	0.517
A4477	Strong	51.7	0.259
A4476	Strong	103.4	0.517
A4474	Strong	172	0.862
A4473	Strong	414	2.068

Table 2: Experimental conditions for nuclear-heated flows

For the sake of brevity, only some of the results for ex-

Pulse	t_p (ms)	t_s (ms)	Q_0 (kW/cm^3)
Weak	75.06	9.13	0.026
Strong	52.30	4.50	0.130

Table 3: Experimental conditions for weak and strong pulses in nuclear-heated flow.

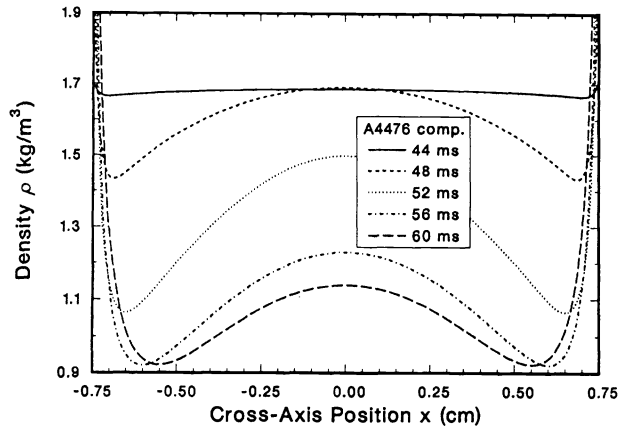

Figure 4: Computed density profiles for experiment A4476.

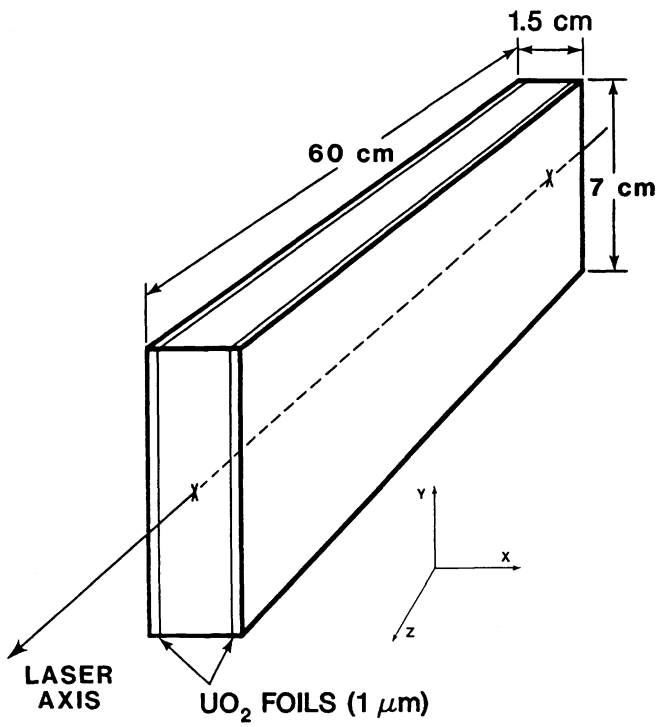

Figure 3: The nuclear-reactor-pumped laser cell is a rectangular box into which gas is introduced through fill lines attached to the cell ends (not shown).

periment A4476 are presented here. Figure 4 shows the computed cross-axis density profiles in the laser cell at selected times during heating. The central region of the cell is seen to be a focusing quadratic duct, whereas the regions adjacent to the side walls deflect ray paths outward (these "boundary layers" form because thermal conduction cools the gas near the side walls). The strength of this quadratic duct grows early on during the heating, but begins to decrease as heating progresses. This is because the cross-axis extent of the thermal boundary layers increases with time, weakening the focusing power of the central region.

Figures 5 and 6 show comparisons of the angular deflections (wavefront slopes) at the exit plane of the laser cell determined using the wavefront sensor with those determined from the computed density gradients. These large values of wavefront slope would be very difficult to measure with an interferometer, but are easily within the dynamic range of the wavefront sensor.

In Fig. 5, the time variations are compared at selected cross-axis positions, whereas Fig. 6 shows the cross-axis variations at selected times during heating. The quantitative agreement is only fair for this case, with the model correctly capturing spatial and temporal variations but systematically overpredicting the wavefront slopes. Although this overprediction is seen in each of the other five cases, agreement is somewhat better for experiments A4435, A4477, and A4474, and fairly good for experiments A4438 and A4473. Torczynski and Neal presented evidence suggesting that this systematic overprediction resulted from the fact that the model allowed spatial variations in only the x direction: gas motion in the y direction, observed with the wavefront sensor, was not incorporated into the model, which would result in artificially high model results[7].

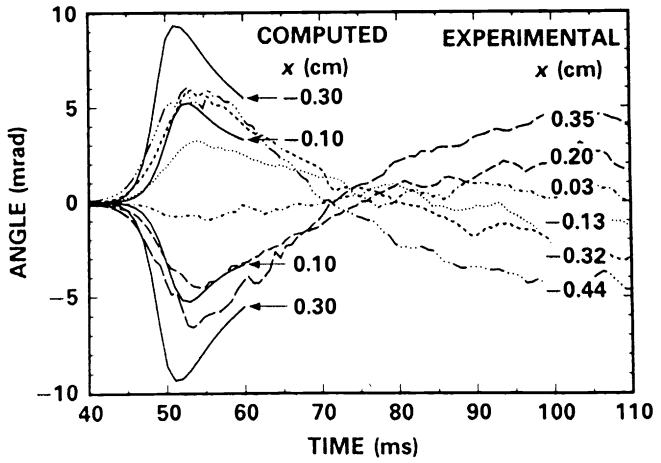

Figure 5: Computed and experimental angular deflections (wavefront slopes) at selected cross-axis positions as functions of time for experiment A4476.

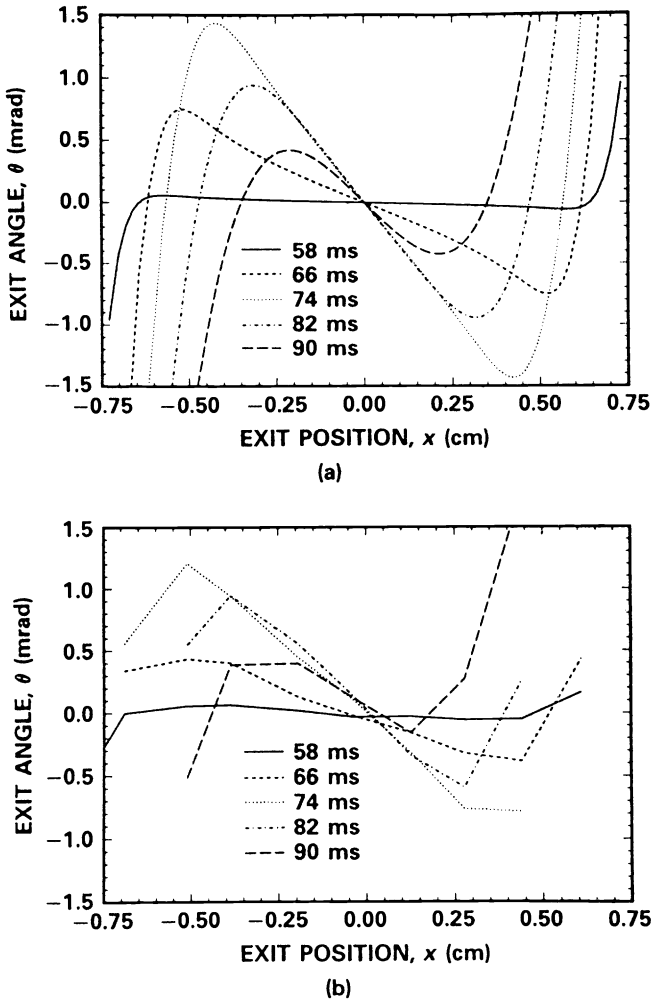

Figure 6: Computed (a) and experimental (b) angular deflections (wavefront slopes) at selected times as functions of cross-axis position for experiment A4476.

3.2 Grid turbulence measurements

Screens are widely used for turbulence control in flowing systems. Understanding of the decay rate of turbulent fluctuations downstream of screens is needed to properly design a turbulence suppression system. The wavefront sensor has been applied to examine the flow downstream of electrically heated screens and the flow downstream of unheated screens subjected to an imposed incoming temperature gradient[3].

Background measurements with no heating show that the rms wavefront slope increases from about 1 μrad to about 2 μrad simply by starting a 17.9 m/s flow. Subsequent experiments demonstrated the effect of increasing the number of heated upstream screens. Rather than a random variation of angle with time, these figures show a strong sinusoidal component at a frequency of 120 Hz with amplitudes of 4–8 μrad, as seen in Fig. 7. Since the screens are electrically heated with 60 Hz AC current, the input electrical power has a sinusoidal component at frequency 120 Hz. This sinusoidal heating term is imposed on the gas temperature, and the resultant temperature variation is convected downstream. This induces a 120 Hz temporal variation in the wavefront slope at a fixed position. These results demonstrate the sensitivity of the wavefront sensor technique: the maximum AC temperature deviations from the mean are ± 0.3°C.

While this work is primarily focused on characterizing the density variations downstream of a uniformly heated screen, i.e. one that produces no mean cross-stream temperature gradients of significantly larger extent than the wire separation M, cross-stream temperature gradients are also important. Since turbulent velocity fluctuations can interact with cross-stream temperature (density) gradients to produce density fluctuations, it is important to assess the magnitude of density fluctuations produced in this manner.

To determine the interaction of the turbulence produced by a screen with an imposed temperature gradient, a triangular array of heating wires is used as depicted in Fig. 8. With this arrangement, temperature gradients with values up to 80°C/cm were produced. Isolation of the temperature gradient effects from the turbulence produced by a flow-scale setting (FSS) screen can be done by using the wavefront sensor to measure only the time-dependent fluctuations which grow in amplitude and scale downstream. Figure 9 shows a typical realization of turbulence from a temperature gradient flow. Experiments were performed to measure the rms wavefront slope at varying downstream distances from the FSS screen. Two sets of experiments were performed, using 16 and 30 mesh FSS screens. The rms wavefront slope and the power spectrum were deter-

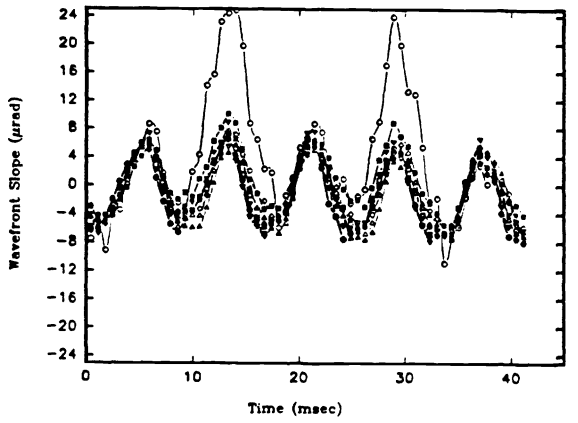

Figure 7: Wavefront slope vs. time: 17.9 m/s; 6.3, 6.0, 6.2, 1.1, and 4.7 kW applied to screens 1–5, respectively.

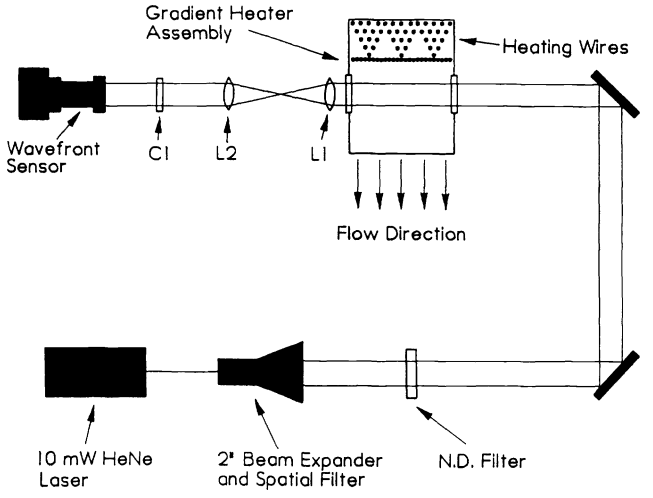

Figure 8: Schematic diagram of wavefront sensor set up to examine flow with large temperature gradients.

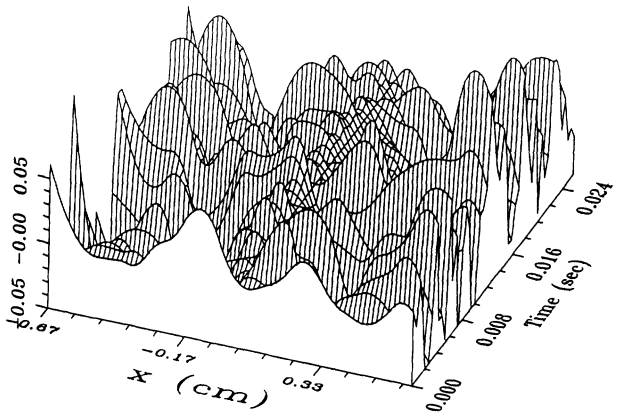

Figure 9: Grid turbulence measured in the presence of an 80°C/cm cross-stream temperature gradient.

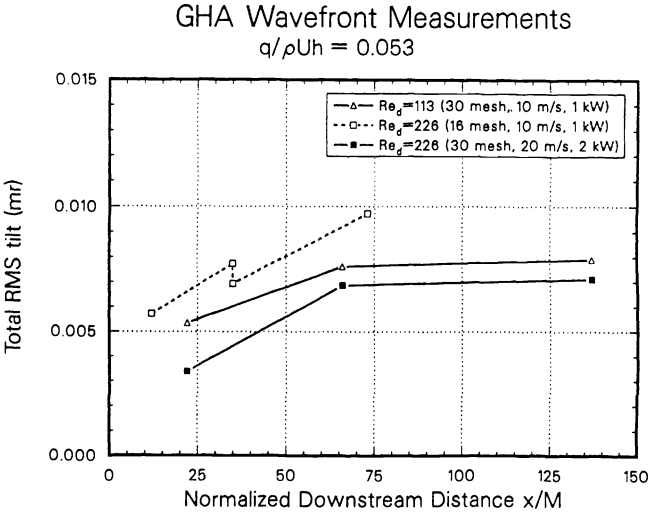

Figure 10: Total rms tilt vs. downstream distance for the two FSS screen meshes.

mined using a 20 element, 10 cm focal length wavefront sensor with the magnification varied to assure adequate resolution.

Figure 10 presents the total rms tilt as a function of downstream distance for the two FSS screens. The larger-scale turbulence generated by the 16 mesh screen decays less rapidly as it propagates downstream and so has a larger rms value at a given downstream location. Similar results were obtained for a case with twice the heating, except that the total rms tilt was higher, ranging from 6 to 18 μrad.

Since these measurements are thought to be resolved, an examination of the power spectrum should yield information about the dominant cell size. The power spectrum can be produced by analyzing the time-dependent data. Figure 11 presents the wavefront-slope power spectrum for different magnifications for the 16 mesh and 30 mesh FSS screens with the wavefront sensor imaged 70 mm downstream. The curves corresponding to a magnification of Mag = 1.5 may suffer from some aliasing due to marginal undersampling of the process.

The total turbulence power is represented by the areas under the curves, which are equal to the squares of the rms values. From a comparison of Figs. 11(a) and 11(b), it is clear that total turbulence power reduces with increasing mesh number. For the 16 mesh FSS screen, Fig. 11(a) shows that most of the turbulence power is located in the frequency range 0.2–0.5 cycle/mm, which corresponds to turbulence structure sizes in the range 2–5 mm. Since the mesh size is about $M = 1.5$ mm, the turbulence power lies in structures significantly larger than the mesh size. Similarly, most of the turbulence power lies in structures larger than the mesh size for the 30 mesh screen, as seen in Fig. 11(b). In this case, the turbulence structure size lies

in the range 2.5–10 mm, whereas mesh size is only M = 0.8 mm.

It is not altogether unexpected that the turbulence scale turns out to be larger than the mesh size M since coalescence of jets can produce flow structures considerably larger than the screen mesh[11]. However, a somewhat surprising observation is that the turbulence structures are larger (although weaker) for the 30 mesh case than for the 16 mesh case. Both measurements were taken 70 mm downstream, so the normalized downstream distance x/M has a value of 83 for the 30 mesh case but a value of only 44 for the 16 mesh case. Since the evolution of the turbulence depends on x/M, the larger value for x/M in the 30 mesh case would provide more opportunity for wake interactions to occur and might thus produce larger structures. Additionally, it is known that smaller turbulence structures viscously decay with time, so more decay of small structures should have occurred for the 30 mesh case than for the 16 mesh case.

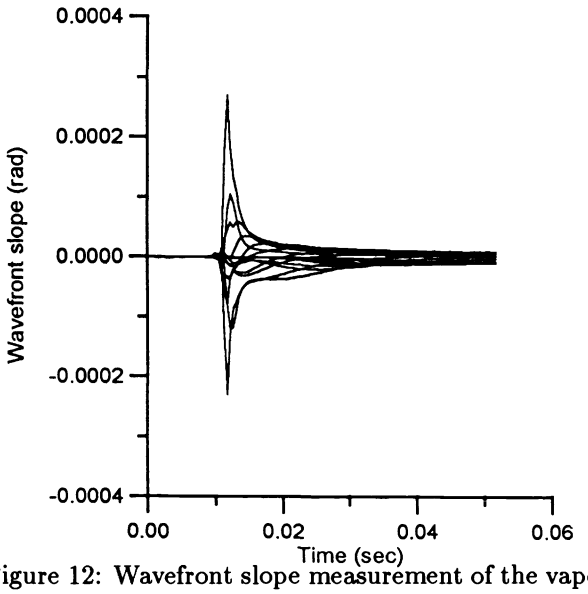

Figure 12: Wavefront slope measurement of the vapor field surrounding an evaporating acetone droplet falling at 1.7 m/s.

3.3 Droplet evaporation

As a final example of wavefront sensor applications, we considered their use for measuring the vapor field surrounding an evaporating droplet. This is an area that has been extensively studied using other techniques[2]. It has extensive applications for all liquid-fueled systems.

The experimental arrangement for droplet evaporation consists of allowing the droplet to fall through a laser beam that is incident upon the wavefront sensor. As the liquid from the droplet evaporates, it changes the refractive index of the surrounding medium. Even though this modulation is rather weak, it is easily detected by the wavefront sensor. Figure 12 depicts the wavefront slope as a function of time for a drop that has fallen through the laser beam. By integrating this measurement, the vapor field can be directly interpreted. This is depicted in Fig. 13. Since the falling droplet effectively scans past the fixed laser beam, this figure represents the full vapor field surrounding the droplet (except for a small correction due to the acceleration and any change in droplet size from evaporation). Note that although the total wavefront error in this figure is only about 0.1 μm, the signal-to-noise ratio is large. These data were acquired with a 40 element wavefront sensor (described further in section 4.1).

4. WAVEFRONT SENSOR ENHANCEMENTS

4.1 Binary optics lenslet array

One of the chief limitations of Shack-Hartmann wavefront sensing is the spatial resolution. Using conventional optical fabrication techniques, we have fabricated 10 and 20 element linear wavefront sensors. This required the fabrication and assembly of 1/10 and 1/20 inch diameter optics. Assembly and handling of these small optics was extremely difficult and tedious, and resulted in inaccurate spacing of the focal spots (which could be calibrated out). To further improve the resolution, a monolithic method was needed for constructing the lenslet arrays.

One such technique relies on the use of binary optics[12] to construct a discrete-level lenslet array on a fused silica substrate. The lenslet array is constructed using photolithography and a series of reactive-ion etch steps to remove material from selected portions of the substrate. The lenslet array profile is built up through successive etch steps, each being twice the depth of the last. Thus four photolithography/etch steps will produce a lens profile with 16 levels. A sixteen-level phase structure can be shown to be more than 99% efficient at focusing light.

We have constructed several lenslet arrays using this technology. They have 40 lenslets across one inch with 10 or 7.6 cm focal length. Several lenslet arrays can be built on a single substrate. Figure 14 presents a surface profile of a portion of one of these lenslet arrays.

A further advantage to the binary optics techniques is the accuracy of lenslet placement. The focus spots are accurately positioned to within 0.5 μm (compare to a typical 13 μm pixel spacing). This allows the use of the sensor in an absolute mode for measuring optical components (or other absolute wavefront measurements). The alignment insensitivity of the wavefront sensor can be maintained if the average tilt is subtracted from the measured wavefront slope values.

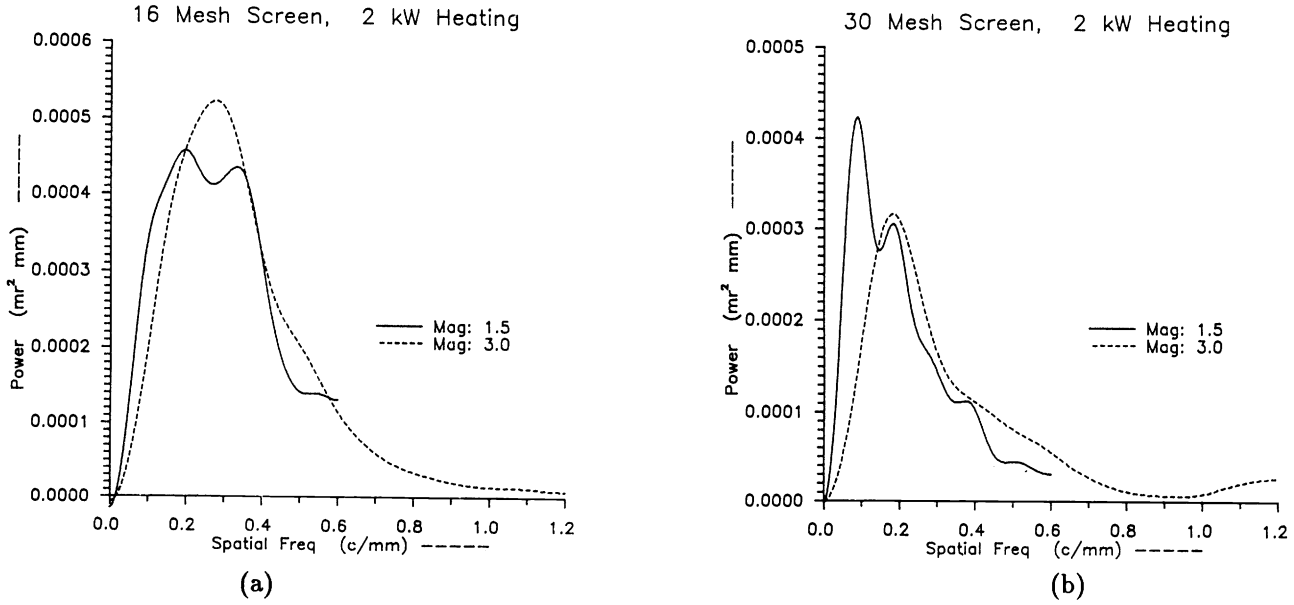

Figure 11: Power spectral density of wavefront slope for various magnifications with 2 kW applied heating power: (a) 16 mesh, (b) 30 mesh.

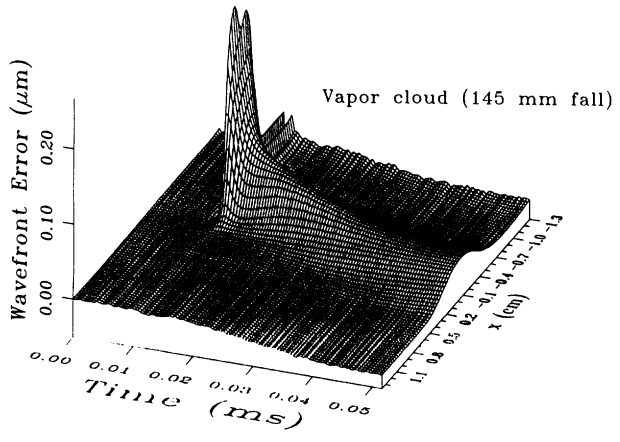

Figure 13: Three-dimensional representation of the droplet vapor field for an acetone droplet falling at 1.7 m/s.

4.2 Frame grabber data acquisition and control

To make effective use of a wavefront sensor for laser system adjustment, the system will need to operate in real (or near real) time. Thus a separate data acquisition/data analysis approach will not be practicable, and the two must be integrated together. This can be done using a frame grabber board that is compatible with a line scan camera for data acquisition and control of the camera, and integrated software for data analysis. Since many frame grabber boards have a digital signal processing (DSP) chip on board, much of the analysis can be performed without ever transferring data to the host PC. It has been found that the most time-consuming portion of the data analysis is finding the centroids of the various focal spots. This operation is very easily performed by the DSP chip at very high rates.

We have begun the development of an integrated data acquisition/analysis environment using an EPIX 4 Meg Video (Model 10) frame grabber board with a TMS320C30 DSP chip. The frame grabber will perform data acquisition, camera timing control, and centroid computation, with the display and other menu functions controlled by the PC. The application will run as a complete Microsoft Windows application.

5. CONCLUSIONS

We have developed a linear Shack-Hartmann wavefront sensor that has high temporal bandwidth, dynamic range and sensitivity. The sensor has a typical noise limit of less

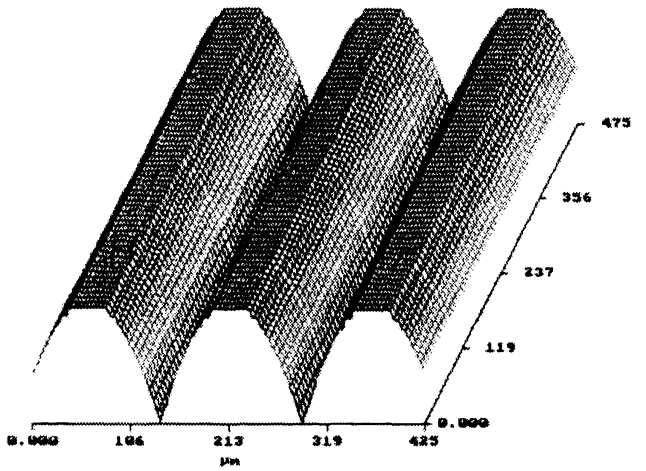

Figure 14: 40 element lenslet array surface profile measurement.

than 1/1000 of a wave simultaneous with a 7–10 wave dynamic range. We have used this sensor to make direct measurements of volumetrically heated flows, fine-scale grid turbulence and droplet vapor evaporation. It can be applied to a large number of fluid dynamics measurements with simple setup and analysis. We have begun several improvements to allow easier data acquisition and analysis, along with greater spatial resolution.

6. ACKNOWLEDGMENTS

The authors would like to thank J. Gruetzner for help with figures and text and WYKO Corporation for lenslet array characterization. This work was performed at Sandia National Laboratories, supported by the U. S. DOE under contract number DE–AC04–76DP00789.

7. REFERENCES

1. Sutter, L., Baily, P., Wakalopulos, G., Hill, R., Peressini, E., Dolezal, F., "Holographic interferometry of a large bore cw high energy gas laser medium during laser power extraction," *Appl. Optics* **18**, 3835–3837, (1979).

2. Neal, D. R. and Baganoff, D. "Laser induced fluorescence measurement of vapor concentration surrounding evaporating droplets," SPIE Vol. 540, *Southwest Conference on Optics*, 347–355 (1985).

3. O'Hern, T. J., Shagam, R. N., Neal, D. R., Suo-Anttila, A. J. and Torczynski, J. R., "Downstream Evolution of Turbulence from Heated Screens: Experimental and Analytical Results," Sandia Report SAND92–0480 (1992).

4. McDaniel, Jr., J.C., Ph.D. Thesis, Department of Aeronautics and Astronautics, Stanford University (1982).

5. Fugate, R., "The current status of the Starfire Optical Range adaptive optics system," SPIE Vol. 1920, *Active and Adaptive Optical Components and Systems II* (1993).

6. Acton, D. and Smithson, R., "Solar imaging with a segmented adaptive mirror," *Appl. Optics*, **31**(16), 3161–3169 (1 June 1992).

7. Torczynski, J. R. and Neal, D. R., "Transient gas motion in nuclear-reactor-pumped lasers: computational and experimental results," *Nucl. Sci. Eng.* **113**, 189–206 (1993).

8. Schmutz, L., "Hartmann sensing at Adaptive Optics Associates," SPIE Vol. 779, *Electromechanical System interaction with Optical Design*, 13–17 (1987).

9. Kwo, D., Damas, G. and Zmek, W., "A Hartmann-Shack wavefront sensor using a binary optic lenslet array," SPIE Vol. 1544, *Miniature and Micro-Optics Fabrication and System Applications*, 66–74 (1991).

10. McKechnie, T. S., "Atmospheric turbulence and the resolution limits of large ground-based telescopes," *J. Opt. Soc. Am. A*, **9**(11), 1937–1954 (1992).

11. Böttcher, J. and Wedemeyer, E., "The flow downstream of screens and its influence on the flow in the stagnation region of cylindrical bodies," *J. Fluid Mech.* **204**, 501–522 (1989).

12. Swanson, G. J., "Binary Optics Technology: The Theory and Design of Multi-Level Diffractive Optical Elements," *MIT Lincoln Laboratory DARPA Technology Report 854* (1989).